

# Small-Signal Average Switch Modeling and Dual-Loop Control of Bidirectional Integrated Converter for G2V and V2G Applications in Battery EVs

Shahid Jaman<sup>1,2</sup>, Sajib Chakraborty<sup>1,2</sup>, Mohammed El Baghdadi<sup>1,2</sup>, Thomas Geury<sup>1,2</sup> and Omar Hegazy<sup>1,2\*</sup>

<sup>1</sup>Vrije Universiteit Brussel (VUB), ETEC Department & MOBI Research Group, Pleinlaan 2, 1050 Brussels, Belgium

<sup>2</sup>Flanders Make, 3001 Heverlee, Belgium

\*E-mail: Omar.hegazy@vub.be

## Acknowledgments

This work was supported by the Horizon 2020 Programme of the European Commission under grant agreements no. 875131 (eCharge4Driver project). We, as authors, also acknowledge Flanders Make for the support to our research group.



## Keywords

«Integrated Converter», «Bidirectional», «Small-Signal», «G2V», «V2G», «Electric Vehicle»

## Abstract

This paper proposes a small signal modeling approach of a bidirectional integrated converter configuration, which utilizes the traction inverter, motor windings and interleaved DC/DC converter for charging applications. This modeling technique represents the power electronic converters (AC/DC and DC/DC) as a transfer function that facilitates both Grid-to-Vehicle (G2V) and Vehicle-to-Grid (V2G) operations. During the G2V mode, the traction inverter converts into an AC/DC converter, while during the V2G mode, it operates as a DC/AC inverter, and the 3-phase interleaved DC/DC converter operates in buck and boost modes for the G2V and V2G operations, respectively. Moreover, the controller design based on the plant transfer functions is also a focal point of this paper. The inner current and outer voltage loop controllers of the DC/DC converter are designed based on the k-factor approach. For DC-link voltage control of the AC/DC converter, a dual loop control approach is adopted. Finally, the performance of both control systems has been validated via performance comparison between switch-based model and small-signal average system model in MATLAB/Simulink®.

## Introduction

Researchers have been already implementing bidirectional configurations where the motor drive is merged with the battery charging system, and the motor coil is utilized as a grid filter [1]-[3]. In such a case, the motor winding utilized as a grid filter inductor in series provides higher inductance without adding the external inductors and guarantees the torque-free operation without any circulating current [1]. It is possible to achieve 65% power density improvement, 30% weight reduction with integrated converter topologies via utilization of next-generation power electronics (e.g., SiC and GaN) and integrated motor drive technologies [4]-[6]. According to the state of the art, the state-space averaging techniques are used to model the power electronic (PE) converters which requires a complex matrix manipulation of a large parasitic and passive component network [7]. Moreover, the designed controller based on state-space technique has higher order harmonics which has significant influence on the controller transient response [8]. Furthermore, PE converter modeling based on Lunze Transformation is discussed in [9]-[10]. The drawback of this technique is the complexity of the controller design and it increases with the number of phases of the PE converter.

In this paper, the small-signal average (SSA) approach is utilized for modeling and control schemes designing of a motor drive integrated bidirectional configuration, as discussed in [4]. The transfer functions of a 2-level 3-phase AC/DC traction inverter and a 3-phase interleaved DC/DC converter are utilized. Furthermore, based on the SSA model, the controller parameters for the feedforward control (AC/DC) and dual-loop cascaded control (DC/DC) have been obtained to achieve less overshoot, better stability and faster dynamic response during charging and discharging modes of operation. Finally, a MATLAB/Simulink® simulation validates the dynamic response of the integrated converter model for both G2V and V2G operations.

## Literature Review of Integrated Converter Topology

The AC/DC converter is the core component of an EV battery charger known as an On-Board Charger (OBC). The on-board charger comprises an AC/DC rectification with grid filter and DC/DC conversion to transfer energy from the grid towards the battery [11]. The DC/DC stage of the OBC consists of DC/AC, high frequency (HF) transformer and AC/DC converter. For this reason, conventional bidirectional OBC becomes expensive and lossy due to transformer losses, and efficiency drops due to galvanic isolation [12]-[14]. The vehicle manufacturer solved these problems by designing bidirectional charging with CHAdeMO DC-charging interface [15]. The bidirectional converter topology removed the galvanic isolation and reduced the power stages which leads to a better efficiency. The OBC of different car manufacturers with associated V2X functionalities is depicted in TABLE I.

**TABLE I: State of the Art of OBC Systems of Different Car Manufacturers [16]**

Manufacturer	Car Type	OBC Ratings	Required Charging Rates		V2X Facilities
			AC Charging	DC Charging	
Nissan Leaf	BEV	3.3kW/6.6kW	6.6 (7h)	50 (35min)	V2G (DC), V2H via CHAdeMO
Mitsubishi Outlander	PHEV	3.7kW	3.7 (3h)	22 (20min)	V2H (DC), V2D via extra electronic unit
BMW i3	BEV	11kW	11 (3h)	50 (25min)	Under development
Toyota Prius	PHEV	3.7kW	3.7 (2h 15min)	-	Not Capable
Renault ZOE	BEV	22kW/43kW	22 (2h)/ 43 (45min)	-	Under development
BYD6	BEV	43kW	11 (6h)/ 43 (2h)	-	V2G, V2V, V2D
Tesla Model 3	BEV	15kW	11 (7h)	90 (1h)	-
Hyundai IONIQ	BEV/ PHEV	3.7kW/6.6kW	6.6 (4.5h)	65(45min)	-

\*V2G = Vehicle to Grid, V2V = Vehicle to Vehicle, V2H = Vehicle to Home and V2D = Vehicle to Device

Recently, vehicle manufacturers integrate their charging system with powertrains to reduce the power stage as well as the power conversion modules. Figure 1 depicts a classic EV powertrain and on-board charging system architecture, including the drivetrain power electronics (inverter) and the on-board charging system (rectifier + DC/DC converter) as separate units [3]. A bidirectional integrated OBC system proposed by Continental [4] is shown in Figure 3, comprising a Grid Interface Box containing parts of the grid filter and star-point configuration. The e-Machine is part of the grid filter, the inverter provides AC/DC rectification, and a DC booster adapts the DC-link voltage to charge the battery.

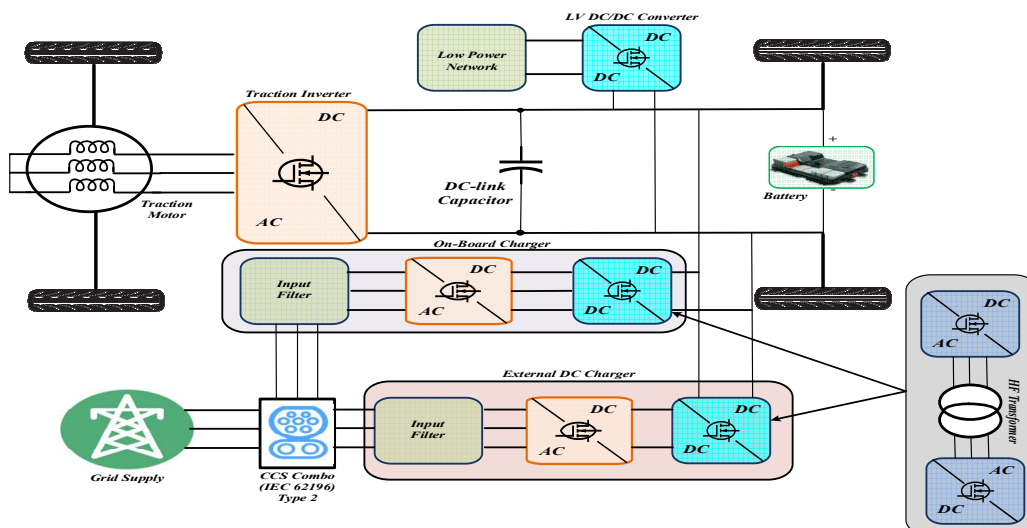


Figure 1: Conventional EV Charging Infrastructure.

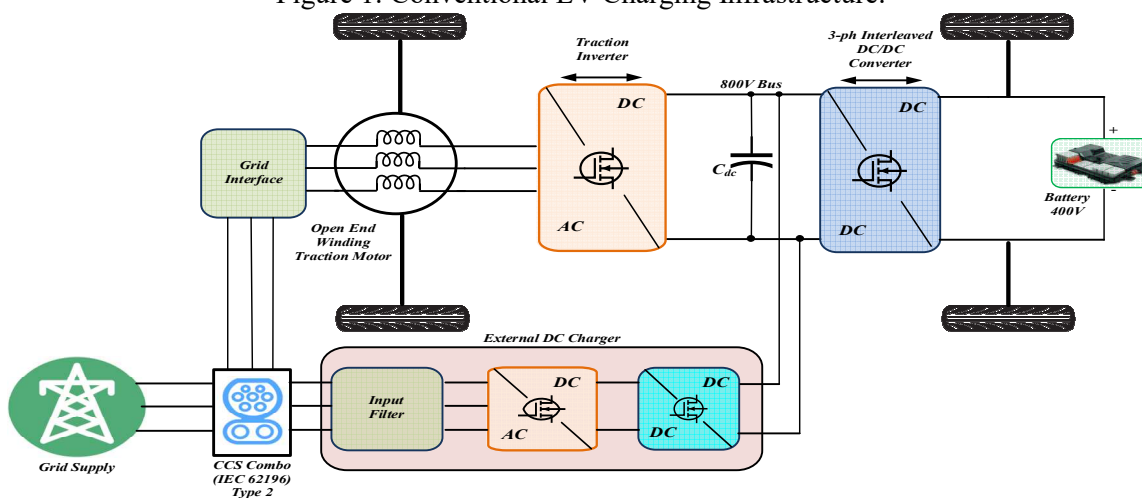


Figure 2: Integrated On-Board Charging Technique to support (400V/800V) Fast Charger by Continental (edited from [3]).

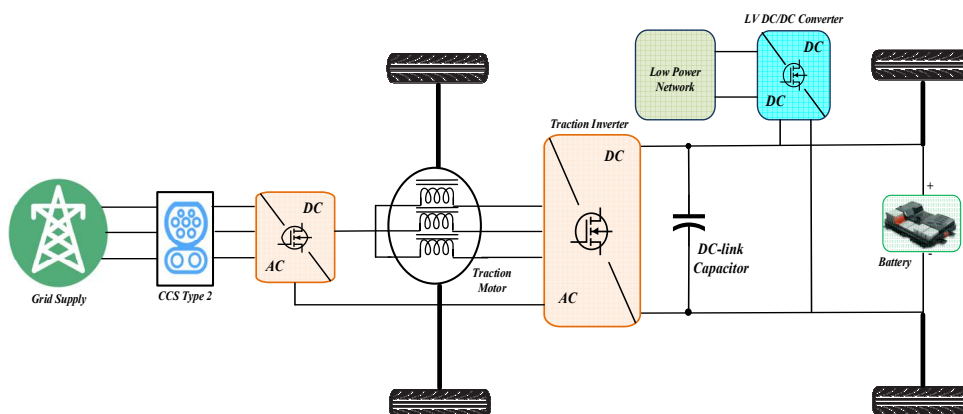


Figure 3: Integrated On-Board Charging Topology for Renault ZOE (edited from [4]).

Additionally, Figure 2 shows the recent architecture of the Renault ZOE Chameleon charging system, which has high power AC integrated charging capabilities up to 43kW [4]. The Chameleon charger comprises the grid connected current-source AC/DC rectifier and 3-phase bidirectional converter. Additionally, the motor windings are utilized as interleaved inductors during charging mode. Thus, the

rectified DC voltage and current go through the star-point of the e-machine to the bidirectional converter, which further adapts the DC link voltage to charge the battery. In this paper, the small-signal average modeling and control technique of an integrated OBC are discussed in detail by considering the G2V and V2G operations.

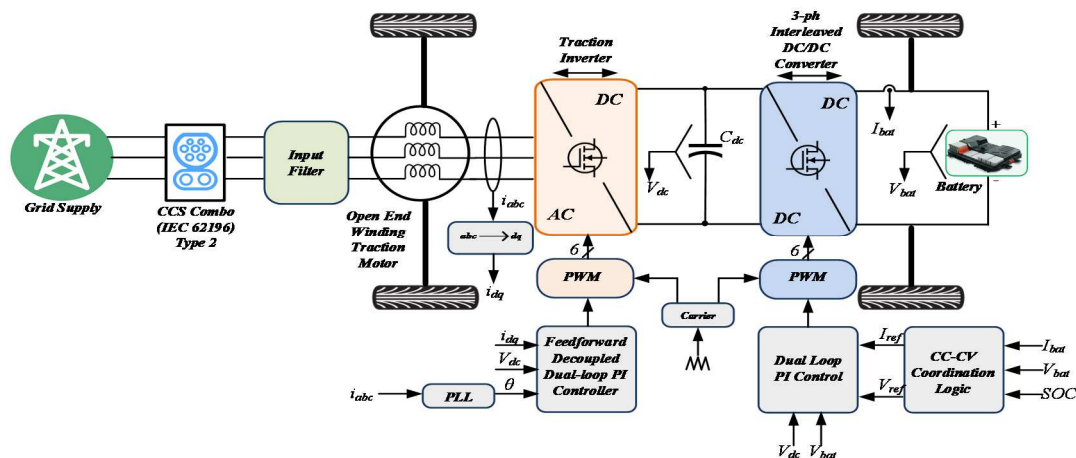


Figure 4: Bidirectional Integrated Charger along with control strategy for the EV applications.

A bidirectional integrated converter topology proposed by Continental (see Figure 4) comprises mainly the traction inverter and 3-phase interleaved bidirectional DC/DC converter with corresponding control techniques. The topology maintains a constant 800-850V DC voltage from the 380Vrms AC input, and the DC/DC converter provides a 400-450V DC voltage to charge the battery. The DC/DC voltage level varies based on the battery voltage response and the operating mode (e.g., G2V and V2G). During the G2V operation, the mentioned traction inverter functions as an active rectifier, and during V2G operation, this converter functions as an inverter. The interleaved DC/DC converter adds the features of DC charging flexibility which means it can support both 400V and 800V fast DC charging.

### Small Signal Average Modeling Technique

Generally, the switching devices consist of transistors and diodes. During continuous current conduction mode (CCM) operation of a PE converter, the transistors and diodes can be replaced by current and voltage-dependent sources, respectively. In this modeling technique, the drain-source voltage and current of a switch are considered as the summation of small-signal and average components. Here,  $i_s$  and  $v_{DS}$  denote the drain-source current and voltage, respectively, and equations (1) and (2) are used as the base of the small-signal average switch modeling technique.

$$i_s = d_T i_L = (d + D)(i_l + I_L) = di_l + Di_l + dI_L + DI_L \quad (1)$$

$$v_{DS} = d_T v_O = (d + D)(v_o + V_O) = dv_o + Dv_o + dV_O + DV_O \quad (2)$$

where  $i_l, I_L$  are the small-signal and average component of the inductor current, and  $d, D$  represent the same for the duty ratio. During the small-signal modeling, the double small-signal terms  $di_l$  and  $dv_o$  can be neglected because  $d \ll D, i_l \ll I_L$  and  $v_o \ll V_O$ .

### Small Signal Transfer Function of Traction Inverter

In Figure 5,  $e_a, e_b$  and  $e_c$  are the 3-phase grid voltages. The mathematical model of an AC/DC converter in the d-q frame is expressed in equation (4)-(5) with the help of matrix T, as shown in equation (3). The small-signal model schematic of the AC/DC converter in CCM mode is shown in Figure 6.

$$T = \sqrt{\frac{2}{3}} \begin{bmatrix} \cos(\omega t) & \cos\left(\omega t - \frac{2\pi}{3}\right) & \cos\left(\omega t + \frac{2\pi}{3}\right) \\ -\sin(\omega t) & -\sin\left(\omega t - \frac{2\pi}{3}\right) & -\sin\left(\omega t + \frac{2\pi}{3}\right) \end{bmatrix} \quad (3)$$

$$v_d = e_d - L_s \frac{di_d}{dt} - r_s i_d + \omega L_s i_q \quad (4)$$

$$v_q = e_q - L_s \frac{di_q}{dt} - r_s i_q - \omega L_s i_d \quad (5)$$

where  $\omega$  is the frequency,  $L_s$  is the input inductance,  $r_s$  is the inductive resistance,  $v_d, v_q$  are the d-q components of supplied voltage at the converter terminal, and  $i_d, i_q$  are the input currents in the d-q frame.

As the system is nonlinear and time-invariant, the small-signal model is developed based on the average signal model [17]. The equations in TABLE II can be expressed in matrix form, as illustrated in equations (6) and (7) with average and small-signal components:

$$\frac{d}{dt} \begin{bmatrix} i_d \\ i_q \end{bmatrix} = \frac{1}{L_s} \begin{bmatrix} e_d \\ e_q \end{bmatrix} - \frac{1}{L_s} \begin{bmatrix} D_d \\ D_q \end{bmatrix} v_{dc} - \frac{1}{L_s} \begin{bmatrix} d_d \\ d_q \end{bmatrix} V_{dc} - \begin{bmatrix} r_s & -\omega \\ \omega & r_s \end{bmatrix} \begin{bmatrix} i_d \\ i_q \end{bmatrix} \quad (6)$$

$$\frac{dv_{dc}}{dt} = \frac{3}{2C} \begin{bmatrix} D_d \\ D_q \end{bmatrix}^T \begin{bmatrix} i_d \\ i_q \end{bmatrix} + \frac{3}{2C} \begin{bmatrix} d_d \\ d_q \end{bmatrix}^T \begin{bmatrix} I_d \\ I_q \end{bmatrix} - \frac{v_{dc}}{CR_L} \quad (7)$$

Here,  $v_{dc}$  represents the dc-link voltage,  $C$  is the output capacitance, and  $R_L$  is the load resistance. The transfer functions of d-axis current-to-duty ( $G_{id}^d(s)$ ) and dc-link voltage-to-duty ( $G_{vd}(s)$ ) are shown in equations (8)-(16) [18]. Here, the q component of the current is zero due to a unitary power factor operation.

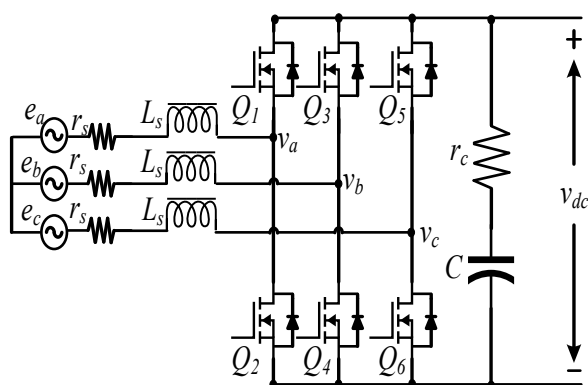


Figure 5: 2-Level 3-ph Bridge AC/DC Converter Switch Model.

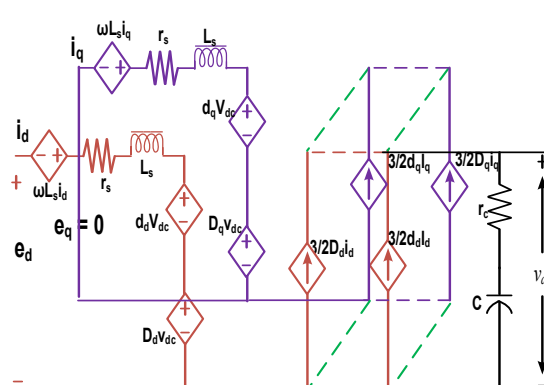


Figure 6: Small-Signal Model of AC/DC Converter.

TABLE II: Mathematical Expressions of Traction Inverter (Rectifier Mode)

	Control to d-axis Current	Control to dc-link voltage
<b>Transfer Functions</b>	$G_{id}^d(s) = \frac{i_d(s)}{d(s)} = G_{di}^d \frac{s + \omega_{zid}}{s^2 + 2\zeta\omega_n s + \omega_n^2} \quad (8)$	$G_{vd}(s) = \frac{v_{dc}(s)}{d(s)} = G_{dv} \frac{s + \omega_{zv}}{s^2 + 2\zeta\omega_n s + \omega_n^2} \quad (9)$
<b>Gain</b>	$G_{di}^d = \frac{4e_d}{L_s C} \quad (10)$	$G_{dv} = \frac{2e_d}{C(1-D)^2} \quad (11)$
<b>Zero</b>	$\omega_{zid} = \frac{2}{C(R_L + r_c)} \quad (12)$	$\omega_{zv} = \frac{3r_c(1-D)^2}{2L_s C} \quad (13)$
<b>Denominator</b>	$s^2 + 2\zeta\omega_n s + \omega_n^2 \quad (14)$	
<b>Natural Frequency</b>	$\omega_n = (1-D) \sqrt{\frac{3r_c}{2L_s C}} \quad (15)$	
<b>Damping Ratio</b>	$\zeta = \frac{2}{\sqrt{\omega_n C(R_L + r_c)}} \quad (16)$	

### Small Signal Transfer Function of Interleaved Bidirectional DC/DC Converter

In charging mode, the charging power flows from the dc-link to the battery through the DC/DC converter, as shown in Figure 7. Thus, the dc-link voltage acts as input to the converter, and the battery side (low voltage) operates as output and vice versa. Therefore, the DC-DC converter works in buck mode during the G2V operation and boost mode during the V2G operation. The small-signal model of the 3-phase interleaved DC/DC converter is expressed in equations (17)- (35) in TABLE III [19]-[20]. The small-signal model schematic of the DC/DC converter in CCM is shown in Figure 8.

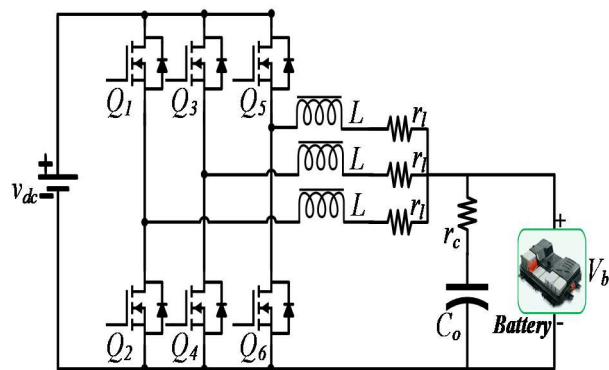


Figure 7: 3-ph Interleaved DC/DC Converter Switch Model.

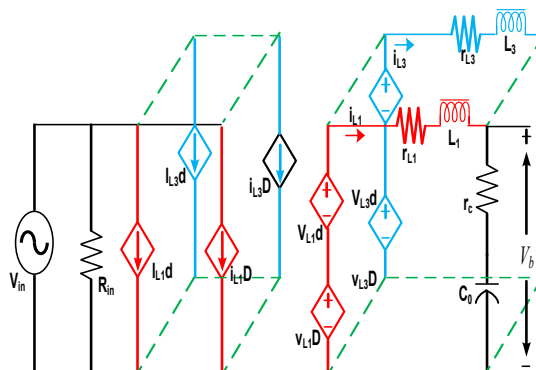


Figure 8: Small-Signal Model of DC/DC Converter.

**TABLE III: Mathematical Expressions of DC/DC Converter (G2V and V2G Mode)**

	Control to inductor Current	Control to Output voltage
<b>Transfer Functions</b>	$G_{id}(s) = \frac{i_L(s)}{d(s)} = G_{di} \frac{s + \omega_{zi}}{s^2 + 2\zeta_{CH}\omega_n^{CH}s + (\omega_n^{CH})^2}$ (17)	$G_{vd}(s) = \frac{v_o(s)}{d(s)} = G_{dv} \frac{s + \omega_{zv}}{s^2 + 2\zeta_{CH}\omega_n^{CH}s + (\omega_n^{CH})^2}$ (18)
<b>Gain</b>	$G_{di} = \frac{V_o}{DL}$ (19)	$G_{dv} = \frac{V_o R_o r_c}{3D(R_o + r_c)}$ (20)
<b>Zero</b>	$\omega_{zi} = \frac{1}{(R_o + r_c)}$ (21)	$\omega_{zv} = \frac{1}{C_o r_c}$ (22)
<b>Denominator</b>	$s^2 + 2\zeta_{CH}\omega_n^{CH}s + (\omega_n^{CH})^2$ (23)	
<b>Natural Frequency</b>	$\omega_n^{CH} = \frac{C_o(r_l R_o + r_l r_c + R_o r_c)}{2\sqrt{LC_o(R_o + r_c)(r_l + R_o)}}$ (24)	
<b>Damping Ratio</b>	$\zeta_{CH} = \sqrt{\frac{r_l + R_o}{LC_o(R_o + r_c)}}$ (25)	
<b>DC/DC Converter (V2G Mode)</b>		
	Control to inductor Current	Control to dc-link voltage
<b>Transfer Functions</b>	$G_{id}(s) = \frac{i_L(s)}{d(s)} = G_{di} \frac{(s + \omega_{zi})}{s^2 + 2\zeta_{V2G}\omega_n^{V2G}s + (\omega_n^{V2G})^2}$ (26)	$G_{vd}(s) = \frac{v_{dc}(s)}{d(s)} = G_{dv} \frac{(s + \omega_{zv1})(s - \omega_{zv2})}{s^2 + 2\zeta_{V2G}\omega_n^{V2G}s + (\omega_n^{V2G})^2}$ (27)
<b>Gain</b>	$G_{di} = \frac{V_o}{r_l + 3(1-D)^2 R_o}$ (28)	$G_{dv} = \frac{-V_o r_c}{(1-D)(R_o + r_c)}$ (29)
<b>Zero</b>	$\omega_{zi} = \frac{1}{C_o(R_o + r_c)}$ (30)	$\omega_{zv1} = \frac{1}{C_o r_c}$ (31)
		$\omega_{zv2} = \frac{3(1-D)^2 R_o - r_l}{L}$ (32)
<b>Denominator</b>	$s^2 + 2\zeta_{V2G}\omega_n^{V2G}s + (\omega_n^{V2G})^2$ (33)	
<b>Natural Frequency</b>	$\omega_n^{V2G} = \sqrt{\frac{r_l + 3r_c R_o (1-D)^2}{2LC_o(R_o + r_c)}}$ (34)	
<b>Damping Ratio</b>	$\zeta_{V2G} = \frac{L + C_o[r_l R_o + r_l r_c + 3(1-D)^2 R_o r_c]}{2\sqrt{LC_o(R_o + r_c)[r_l + 3(1-D)^2 R_o]}}$ (35)	

## Controller Design Approaches

### Controller Design for Bidirectional Interleaved DC/DC Converter

A cascaded structure of control system for bidirectional interleaved DC/DC Converter is shown in Figure 9. It comprises an outer voltage loop and an inner current loop which is ten times faster than the voltage loop.

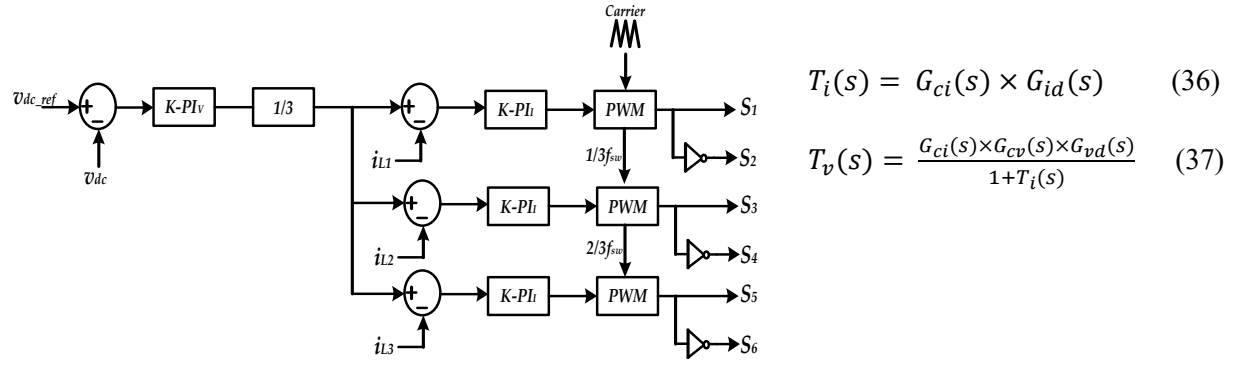


Figure 9: Dual Loop Control Structure of Interleaved Bidirectional DC/DC Converter with PWM.

The fast-inner loops are used to regulate the average inductor currents,  $i_{L1}$ ,  $i_{L2}$  and  $i_{L3}$  using k-factor based lead-lag controllers. The continuous duty ratios from the controllers are then sent to the PWM modules for the generation of the switching signals for six power semiconductor modules. A phase shift of  $1/3f_{sw}$  is added between adjacent PWMs for interleaved switching. The output voltage is controlled using the slower outer loop, also with a lead-lag controller. The advantage of the dual loop is that it decouples the two loops and requires only a single lead-lag controller per loop. The precise design of these controllers depends on the adapted control algorithm technique. The type-II ‘k-factor’ approach is well-established in the literature for the design methodology of the PI controllers [21]. The controller structures are shown in equation (38). The controller loop gain  $K_c$  has been calculated using equations (36) and (37). The design procedure of ‘k-factor’ approach is depicted in equations (39)-(44).

$$\text{Type II Controller Structure: } G_c^{II} = K_c \frac{1 + \frac{s}{\omega_z}}{s(1 + \frac{s}{\omega_p})} \quad (38)$$

**Step 1:** Select 0-dB crossover frequency for compensated system. Typically,  $f_c = \frac{f_{sw}}{10}$  (39)

**Step 2:** Select phase margin  $\varphi_{mg}$  for closed loop system which is typically  $60^\circ$ .

**Step 3:** Calculate phase boost  $\varphi_{bo}$ .  
 $\varphi_{bo} = -90 + \varphi_{mg} - [\varphi_G(f_c) - 360^\circ]$  (40)

**Step 4:** Calculate k-factor  $K_{bo}$ .

$$K_{bo} = \left| \tan\left(\frac{\varphi_{bo}}{2} + 45^\circ\right) \right| \quad (41)$$

**Step 5:** Calculate pole-zero location  $\omega_z$  and  $\omega_p$ .

$$\omega_p = K_{bo} \times 2\pi f_c \quad (42)$$

$$\omega_z = \frac{2\pi f_c}{K_{bo}} \quad (43)$$

**Step 6:** Calculate controller gain  $K_c$ .

$$K_c = \left| \frac{1}{T(s)} \right|_{f=f_c} \quad (44)$$

The calculated controller transfer functions of DC/DC converter for both G2V and V2G operations is given in TABLE IV below:

TABLE IV: Type-II Controller Transfer Function for G2V and V2G Operation

G2V Operation		V2G Operation	
Voltage Controller	Current Controller	Voltage Controller	Current Controller
$G_{cv}(s) = \frac{s + 1942}{0.00021s^2 + 0.3891s}$	$G_{ciL\_Buck}(s) = \frac{s + 5351}{0.002s^2 + 133.5s}$	$G_{cv}(s) = \frac{s + 2504}{0.00025s^2 + 0.972s}$	$G_{ci}(s) = \frac{s + 4634}{0.0032s^2 + 167.2s}$

### Controller Design for Active front end (AFE) Converter

The controller design of the AFE converter is discussed in this section. The dual-loop control approach is used and comprises the outer voltage control loop and inner current loop for the d-axis and q-axis current control [22]. Equations (4) and (5) depict that it is possible to obtain  $v_d$  and  $v_q$  by adjusting  $i_d$  and  $i_q$ , respectively. The  $v_d$  and  $v_q$  references can be calculated by following equations (45) and (46). Therefore, the injected current can be modeled as equations (47) and (48). Finally,  $v_d$  and  $v_q$  can be

expressed as functions of  $v_d^*$ ,  $v_q^*$  and  $i_d$ ,  $i_q$  which is shown in equations (49) and (50), where  $K_p$  and  $K_i$  are the proportional and integral gains, respectively.

$$v_d^* = L_s \frac{di_d}{dt} + r_s i_d \quad (45) \quad i_d(s) = \frac{1}{sL_s + r_s} v_d^*(s) \quad (47)$$

$$v_q^* = L_s \frac{di_q}{dt} + r_s i_q \quad (46) \quad i_q(s) = \frac{1}{sL_s + r_s} v_q^*(s) \quad (48)$$

$$v_d = e_d + \omega L_s i_q - \left( K_p + \frac{K_i}{s} \right) (i_d^* - i_d) \quad (49)$$

$$v_q = e_q + \omega L_s i_d - \left( K_p + \frac{K_i}{s} \right) (i_q^* - i_q) \quad (50)$$

The control system of the AFE converter is shown in Figure 10. The formulation of each controller and their optimization is carried out using gain margin at gain margin frequency and phase margin at the crossover frequency. Inner loop current controllers are designed at the crossover frequency of  $1/(10f_{sw})$ , and outer closed-loop voltage control is designed at the crossover frequency of AC line frequency 50Hz. The PI-controller transfer function is shown in equations (51) and (52).

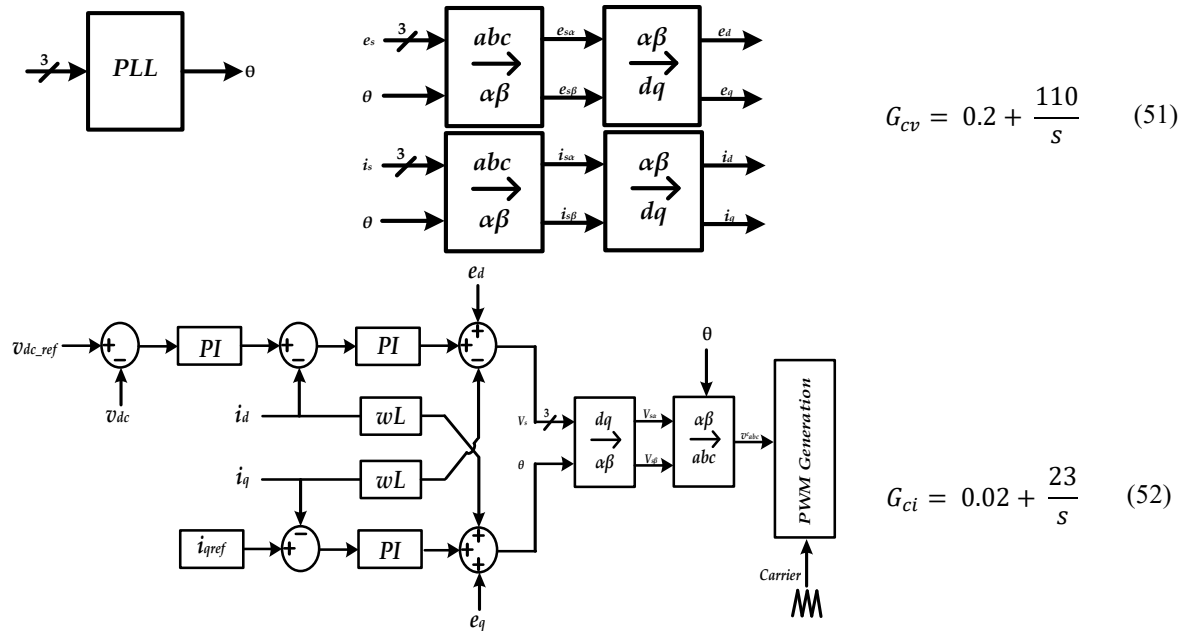


Figure 10: Dual Loop Control Strategy of Active Front-end Converter with PWM

## Simulation Results and Discussion

A simulation model of the integrated bidirectional converter at 30kW nominal power has been implemented in MATLAB/Simulink® platform. The battery specifications of the simulation are given in TABLE V.

Table V. Battery Specifications for Simulation

Description	Values	Description	Values
Battery nominal voltage	390V	Discharging current command (V2G)	35A
Battery capacity	40Ah	Initial state of charge (SoC)	60%
Charging current command (G2V)	75A	G2V and V2G Transition	1sec

In this paper, the inner current loop is 10 times faster in operation than the outer voltage loop for both converters. Both converters are operating in a stable region which is validated by the bode plot. For

instance, Figure 11 and Figure 12 are illustrating the frequency responses of the current and voltage control loops of the DC/DC converter. The faster inner current loop becomes stable with high gain margin and  $60^\circ$  phase margin. Moreover, the slower outer voltage control loop becomes stable with 21.2dB gain margin and  $60^\circ$  phase margin. On the other hand, Figure 13 shows that the direct current  $I_d$  of the AC/DC converter becomes stable after 20ms without overshoot. The switch average and small signal average model performances are shown in Figure 14 where the direct axis current reaches steady state with a settling time of 3.1ms. Therefore, the dc-link voltage, which is the output of the AC/DC converter, is controlled within the specified voltage range.

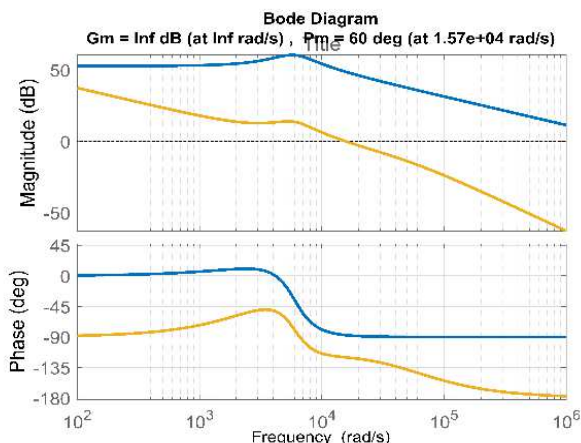


Figure 11: Magnitude plot of Inner Current Loop of DC/DC Converter

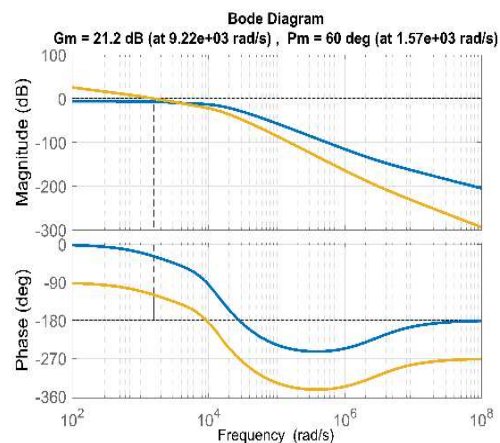


Figure 12: Phase plot of Outer Voltage Loop of DC/DC Converter

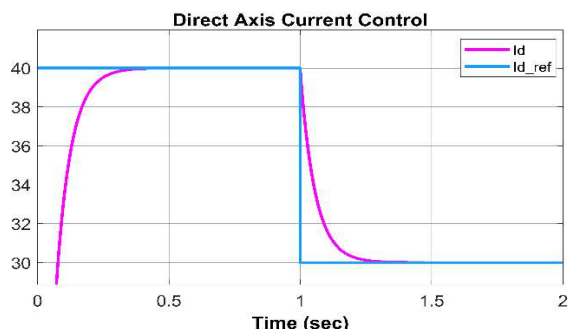


Figure 13: Controller performance during direct current ( $I_d$ ) control

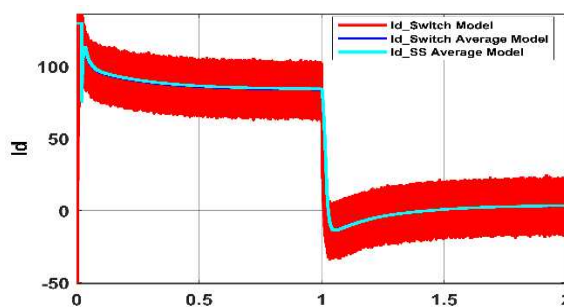


Figure 14: Simulation of direct axis current ( $I_d$ ) with average and switch model.

The battery performances during G2V and V2G are illustrated in Figure 15 and Figure 16. The mentioned figures compare the current and voltage dynamics of the switch average model with the small-signal average model in MATLAB/Simulink. The simulation parameters are listed in TABLE VI. The simulation results verify that the small-signal model explained in above section is valid for any operating condition.

Table VI. Simulation Parameters

Description	Values	Description	Values
DC-link Voltage	850V	Converter Side Inductance	0.18mH
Battery Voltage	450V	Grid Side Inductance	0.2mH
Nominal Power	30kW	Interleaved Inductance	1mH
DC-link Capacitance	640 $\mu$ F	Filter Capacitance	1000 $\mu$ F
Switching Frequency	20kHz	Fundamental Frequency	50Hz

Both the average and the switching models have similar dynamics with a load of 30 kW. Until  $t = 1s$ , the system works in charging mode and absorbs power from the grid. After  $t=1s$ , the mode switches to V2G, and it supplies energy back to the grid. The dc-link voltage is remaining around 850V in both

modes, as shown in Figure 17. The dc-link voltage increases from 850V to 940V at  $t=1s$ . Then the voltage returns to the stable voltage level after 10ms, and the ripple is about 8V.

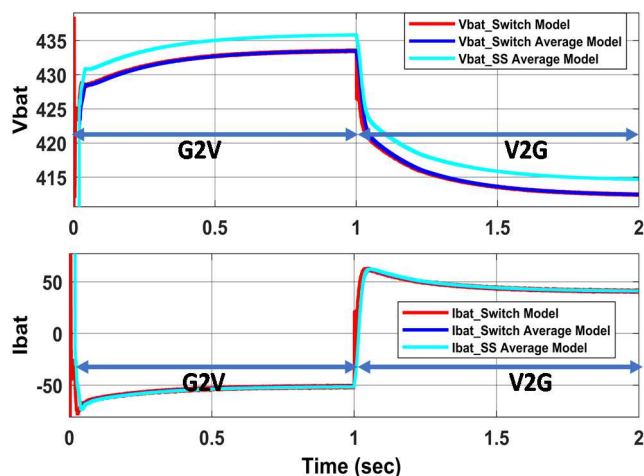


Figure 15: Switch Average Model and Small Signal Model performance of Battery Voltage and Current

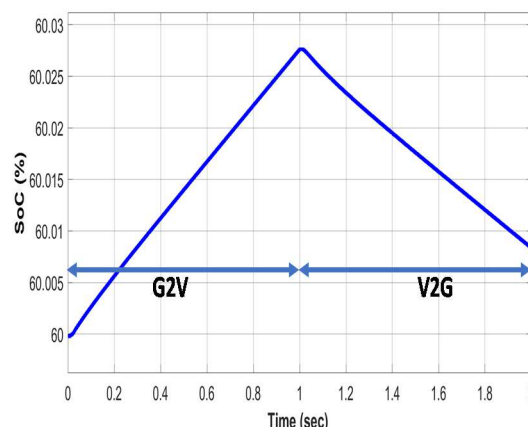


Figure 16: Battery SoC Profile during G2V and V2G Operation

The grid current is around 75Arms flowing through the system during charging which is shown in Figure 18. It can be seen from the figure that the grid current drops at  $t = 1s$  during the transition from G2V to V2G. The THD of the grid current is 6.59% during V2G and 5.34% during G2V operation.

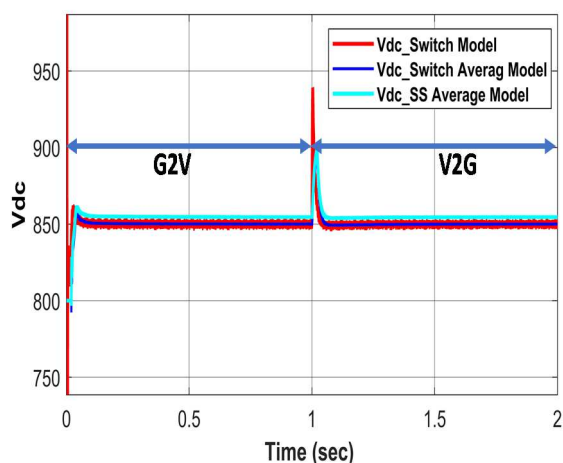


Figure 17: DC-link Voltage Comparison between Switch and Average Model

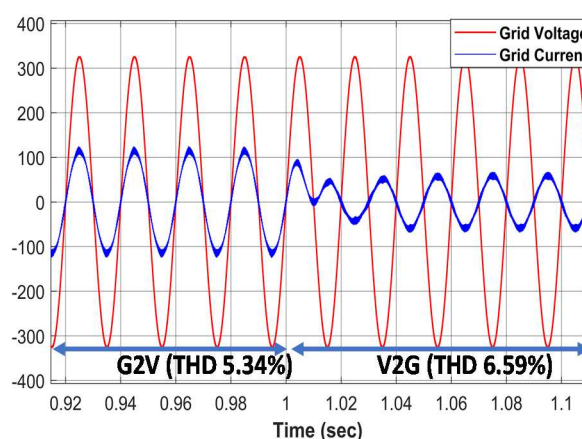


Figure 18: 3- $\phi$  grid currents with THD. The grid current THD is 5.34% (G2V) and 6.59% (V2G)

The controller performances are shown in TABLE VII for both converters. Both PE converter controllers need less than 5ms to stabilize the output response of the PE converters. Moreover, the overshoot of the dual-loop controller for the AFE converter is slightly higher than with k-factor-based controller. A relatively high degree of accuracy has been achieved between switch average and small-signal model results.

Table VII. Controller Performance on Output Voltage Response

	k-factor-based controller		AFE Controller	
	Switch Average Model	Small Signal Average Model	Switch Average Model	Small Signal Average Model
<b>Overshoot</b>	0.33% (1.5V)	0.28% (1.3V)	1.76% (14.96V)	1.34% (11.39V)
<b>Settling Time</b>	3.6ms	2.8ms	3.5ms	3.1ms

## Conclusion

In this paper, an average switch-based small-signal modeling approach of a bidirectional integrated converter for electric vehicle powertrains has been proposed and verified. Moreover, the mathematical formulation of the output voltage-to-duty cycle and inductor current-to-duty cycle transfer functions for 3-phase bridge AC/DC and 3-phase interleaved DC/DC converters with a dual-loop control model has been developed. The dynamic performances and stability of the integrated charger topology for both the G2V and the V2G modes are verified using MATLAB/Simulink®. The comparative simulation study shows that the dc-link voltage ripple is lower than  $\pm 5\%$  for a 30kW load operation and the maximum settling time is lower than 4ms. Furthermore, the THD for grid current is less than 10% for both G2V and V2G operations. These results are verified the feasibility of the proposed small signal model and control performance of a integrated bidirectional converter for electric vehicle application in V2G and G2V mode. In the future, a laboratory prototype of this proposed topology will be prepared for hardware validation and digital twin implementation.

## References

- [1] S. Sharma, M. V. Aware and A. Bhowate, "Integrated Battery Charger for EV by Using Three-Phase Induction Motor Stator Windings as Filter," in IEEE Transactions on Transportation Electrification, vol. 6, no. 1, pp. 83-94, March 2020, doi: 10.1109/TTE.2020.2972765.
- [2] J. Gupta, R. Maurya and S. R. Arya, "Improved Power Quality On-Board Integrated Charger With Reduced Switching Stress," in IEEE Transactions on Power Electronics, vol. 35, no. 10, pp. 10810-10820, Oct. 2020, doi: 10.1109/TPEL.2020.2981955.
- [3] Bruell, Martin & Brockerhoff, Philip & Pfeilschifter, Franz & Feustel, Hans-Peter & Hackmann, Wilhelm. (2016), "Bidirectional Charge- and Traction-System," World Electric Vehicle Journal. 8. 237-248. 10.3390/wevj8010237.
- [4] S. Loudot, B. Briane, O. Ploix, A. Villeneuve "Fast Charging Device for an Electric Vehicle" Renault S.A.S US Patent No. US 20120286740A1, Nov 15, 2012.
- [5] C. Liu, K. T. Chau, D. Wu, and S. Gao, "Opportunities and challenges of vehicle-to-home, vehicle-to-vehicle, and vehicle-to-grid technologies," Proc. IEEE, vol. 101, no. 11, pp. 2409–2427, Nov. 2013.
- [6] Graf F., Brüll M., Deinhard S. (2018) AllCharge™ – a user-centric solution for traction and charging. In: Liebl J. (eds) Der Antrieb von morgen 2018. Proceedings. Springer Vieweg, Wiesbaden.
- [7] A. Skandarnezhad, A. Rahmati, A. Abrishamifar, and A. Kalteh, "Small-Signal Transfer-Function Extraction of a Lossy Buck Converter Using ASM Technique," vol. 2, no. 7, pp. 1760–1763, 2014.
- [8] P. Azer and A. Emadi, "Generalized State Space Average Model for Multi-Phase Interleaved Buck, Boost, and Buck-Boost DC-DC Converters: Transient, Steady-state and Switching Dynamics," IEEE Access, vol. PP, pp. 1–1, 2020.
- [9] H. Shin, J. Park, S. Chung, H. Lee, and T. A. Lipo, "Generalised steady-state analysis of multiphase interleaved boost converter with coupled inductors," IEE Proc. - Electr. Power Appl., vol. 152, no. 3, pp. 584–594, May 2005.
- [10] H. Shin, E. Jang, J. Park, H. Lee, and T. A. Lipo, "Small-signal analysis of multiphase interleaved boost converter with coupled inductors," IEE Proc. - Electr. Power Appl., vol. 152, no. 5, pp. 1161–1170, 2005.
- [11] H. Vu, M. Abdel-Monem, M. El Baghdadi, J. Van Mierlo and O. Hegazy, "Multi-Objective Optimization of On-Board Chargers Based on State-of-the-Art 650V GaN Power Transistors for the Application of Electric Vehicles," 2019 IEEE Vehicle Power and Propulsion Conference (VPPC), 2019, pp. 1-6, doi: 10.1109/VPPC46532.2019.8952196.
- [12] C. Liu, 8. Gu, J. S. Lai, M. Wang, Y. Ji, G. Cai, Z. Zhao, C. L. Chen, C. Zheng, and P. Sun, "High-efficiency hybrid fuH-bridge--half-bridge converter with shared ZVS lagging leg and dual outputs in series, " IEEE Trans. Power Electron., vol. 28, no. 2, pp. 849-861, Feb. 2013.
- [13] M. Yilmaz and P. T. Krein, "Review of banery charger topologies, charging power levels, and infrastructure for plug-in electric and hybrid vehicles, " IEEE Trans. Power Electron., vol. 28, no. 5, pp. 2151-2169, May 2013.
- [14] A. Khaligh and S. Dusmez, "Comprehensive topological analysis of conductive and inductive charging solutions for plug-in electric vehicles, " IEEE Trans. Veh. Technol., vol. 61, no. 8, pp. 3475-3489, Oct. 2012.
- [15] Garcés Quílez, M.; Abdel-Monem, M.; El Baghdadi, M.; Yang, Y.; Van Mierlo, J.; Hegazy, O. Modelling, Analysis and Performance Evaluation of Power Conversion Unit in G2V/V2G Application— A Review. Energies 2018, 11, 1082.
- [16] [https://www.energy.gov/sites/prod/files/2017/06/f34/edt087\\_burress\\_2017\\_o.pdf](https://www.energy.gov/sites/prod/files/2017/06/f34/edt087_burress_2017_o.pdf)

- [17] K. Hartani, M. Bourahla, Y. Miloud, M. Sekour "Control Strategy for Three Phase Voltage Source PWM Rectifier based on the SVM" EFEEA'10 International Symposium on Environment Friendly Energies in Electrical Applications. 2-4 November 2010, Ghardaïa, Algeria
- [18] B. Yin, R. Oruganti, S. K. Panda and A. K. S. Bhat, "A Simple Single-Input–Single-Output (SISO) Model for a Three-Phase PWM Rectifier," in *IEEE Transactions on Power Electronics*, vol. 24, no. 3, pp. 620-631, March 2009, doi: 10.1109/TPEL.2008.2012529.
- [19] O. Hegazy, J. V. Mierlo and P. Lataire, "Analysis, Modeling, and Implementation of a Multidevice Interleaved DC/DC Converter for Fuel Cell Hybrid Electric Vehicles," in *IEEE Transactions on Power Electronics*, vol. 27, no. 11, pp. 4445-4458, Nov. 2012.
- [20] S. Chakraborty, D. -D. Tran, J. van Mierlo and O. Hegazy, "Generalized Small-Signal Averaged Switch Model Analysis of a WBG-based Interleaved DC/DC Buck Converter for Electric Vehicle Drivetrains," 2020 22nd European Conference on Power Electronics and Applications (EPE'20 ECCE Europe), Lyon, France, 2020, pp. P.1-p.8.
- [21] D.D. Tran, G. Thomas, M. El Baghdadi, J. Van Mierlo, and O. Hegazy, "Design and Implementation of FPGA-based Digital Controllers for SiC Multiport Converter in Electric Vehicle Drivetrains," 2019 21st Eur. Conf. Power Electron. Appl. (EPE'19 ECCE-Europe), Genova, pp. 1–7, 2019.
- [22] V. Selarka, P. Shah, D. J. Vaghela and M. T. Shah, "Closeloop control of three phase Active Front End Converter using SVPWM technique," 2016 International Conference on Electrical Power and Energy Systems (ICEPES), Bhopal, 2016, pp.339-344.